

A Study on the Performance of Conditional Generative Adversarial Networks for Reconstructing IR Thermometry in Flow Boiling

UngJin Na ^a, ByongGuk Jeon ^b, JunYoung Seo ^c, HangJin Jo ^{a, d, *}

^aDepartment of Mechanical Engineering, Pohang University of Science and Technology, Pohang, South Korea

^bKorea Atomic Energy Research Institute, Daejeon, South Korea

^cDepartment of Mechanical Engineering, Ajou University, Suwon, South Korea

^dDivision of Advanced Nuclear Engineering, Pohang University of Science and Technology, Pohang, South Korea

* Corresponding author: jhj04@postech.ac.kr

***Keywords : Flow Boiling, Infrared Thermometry, Conditional Generative Adversarial Networks**

1. Introduction

Flow boiling is a critical process in high-efficiency thermal management systems, including refrigeration, microelectronics cooling, and nuclear power plants. As the fluid absorbs heat and transitions to a vapor phase, the heat transfer from the surface is significantly improved, due to the latent heat of vaporization. This process begins with the onset of nucleate boiling (ONB), marking the initiation of bubble formation, and is constrained by the departure from nucleate boiling (DNB), where the boiling surface becomes enveloped by a vapor film, leading to a sharp decline in heat transfer efficiency.

Among contemporary techniques, total reflection visualization and infrared thermography provide important insights into the dynamic and thermal behavior of coalescing bubbles and their expansion, especially when these techniques are used at the same time [1, 2]. The acquired experimental data have significantly enhanced the understanding of boiling phenomena, particularly at the DNB, drawing on results that simultaneously measure the shape and temperature distribution of dry patches formed on the boiling surface. Jeon et al. employed these techniques to observe and analyze the behavior and formation process of bubble structures and dry patches, presenting findings on the thermal criteria of the dry patch periphery at DNB under various testing conditions [3]. Yet, despite the fact that extensive research has been conducted for a long time to elucidate its mechanisms, the understanding of flow boiling heat transfer remains incomplete due to the complex thermal-hydraulic interactions between momentum transfer and heat transfer within the system.

On the other hand, recent advancements in convolutional neural networks (CNNs) have underscored the remarkable proficiency of neural networks in capturing visual features, raising the possibility of simplifying complex experimental setups and data extraction [4]. Particularly with the introduction of generative adversarial networks (GANs), learning the style of input data and generating images has become easier, allowing various image processing tasks to be addressed within a unified framework [5]. Deep convolutional GANs (DCGANs) have enhanced the stability of the learning process and the ability to capture

visual features [6]. Conditional GANs (cGANs) have introduced the capability for rapid image transformations using a convolutional generator and a discriminator architecture [7].

This study presents a cGAN-based approach to learn and identify the potential styles of temperature field at the boiling surface to generate outputs even though the transfer function between the optical visualization and infrared thermometry is not explicitly known. The ablation results of the cGAN networks are presented, focusing on simplifying and facilitating the rapid training and the generation of images by extracting important information from large datasets. The thermographic images produced in this study were compared with experimentally measured infrared thermography images, enhancing the reliability of the research findings.

2. Methodology

2.1 Flow Boiling Data Acquisition and Visualization

The data used in this study consists of total reflection visualization images and infrared thermographic images captured under the conditions of a flow boiling experiment. The main test section of this experiment was made of PEEK with four windows using quartz, pyrex and sapphire. The IR camera faced an Indium Tin Oxide (ITO) heater. The total reflection visualization images were captured using a Memrecam GX-3 high-speed camera, and the infrared imageries were captured using a FLIR X6903sc camera. The experimental conditions are as follows:

Table I: Experimental Conditions

ID	Inlet Temperature	Mass Flow rate	Heat Flux
1	94.5 °C	250 kg/s/m ²	399 kW/m ²
2	95.6 °C	250 kg/s/m ²	796 kW/m ²
3	95.3 °C	249 kg/s/m ²	1197 kW/m ²
4	94.3 °C	249 kg/s/m ²	1549 kW/m ²

Further experimental details can be found in [3].

2.2 Implementation of cGANs

The objective function of mapping total reflection visualization images to infrared thermographic images can be represented as follows:

$$G^* = \arg \min_G \max_D (\mathcal{L}_{cGAN}(D, G) + \mathcal{L}_{L1}(G))$$

Here, \mathcal{L}_{cGAN} denotes the conditional adversarial loss function derived from the output of discriminator and \mathcal{L}_{L1} denotes the L1 loss between the generated image and the ground truth infrared image. The quality of the generated images is improved by the learning process where both the generator and discriminator strive to minimize the objective function, which is expressed as:

$$\mathcal{L}_{cGAN} = \mathbb{E}_{y \sim p_{data}(y)} [\log D(y|x)] + \mathbb{E}_{\hat{y} \sim p_{data}(\hat{y})} [\log (1 - D(G(\hat{y}|x)))]$$

Where the first term represents the expected value of the log probability that the discriminator correctly classifies the actual images (y) based on the condition (x). The second term represents the expected value of the log probability that the discriminator incorrectly identifies the generated images (\hat{y}). This is learned using a binary cross-entropy loss function that compares generated outputs with actual values.

During the training process, the generator attempts to fool the discriminator into believing its produced infrared images are convincing, while the discriminator tries to distinguish between actual and generated infrared images. Through this optimization process, both the generator and discriminator are iteratively updated, allowing the model to effectively learn how to generate realistic images indistinguishable from actual ones. That is, when equilibrium is reached through training, the neural network's generator (G) is trained to transform input images into output images similar to the target. Meanwhile, the discriminator (D) aims to distinguish between actual and generated images, bringing the conditional probability of predictions based on input closer to the conditional probability of actual values based on input.

2.3 Neural Network Structure

In this study, a modified U-Net structure was used as the generative model to create images. The structure of the generator consists of an encoding path and a decoding path. The encoding path comprises a series of downsampling modules that transform the total reflection image domain into a latent space to understand the spatial information of the input image. The decoding path consists of a series of upsampling modules that transform the latent variable back into the infrared thermographic image domain to generate the output image. Skip connections between the two paths help preserve low-level information shared between the input and output.

2.4 Training Principles

The cGAN models are trained by pairing total reflection visualization and infrared thermographic images, aligning with the actual visualization results of boiling experiments. The dataset consists of 1800 images for each of the experimental conditions, with images for the training and test datasets randomly shuffled at a 9:1 ratio. Training was conducted over a total of 100 epochs, and for each training batch, images were generated through a forward pass by the generator, then both the generative adversarial loss and L1 pixel-wise loss were calculated using these images and their corresponding actual images. Based on these loss functions, the weights of the generator were updated, with the learning rate for the generator set to $2e-4$, and the β values for the Adam optimization algorithm set to 0.5 and 0.999. The model was initialized with random variables having a mean of 0 and a standard deviation of 0.02, and the entire model implementation and training were conducted using Python 3.10.4, PyTorch 1.12.0, CUDA 11.3.58, cuDNN 8.2.0, and an RTX3070Ti on an Ubuntu 20.04 system.

2.5 Ablation Test Matrix

The ablation tests of this study are designed to assess the network structure. The depth of the network at the generator varies from 2 to 6, both at the encoder and the decoder sides. Fig. 1 lays out the brief structure of the generator and the discriminator, where the input of the generator is the total reflection image and the output is the infrared thermography.

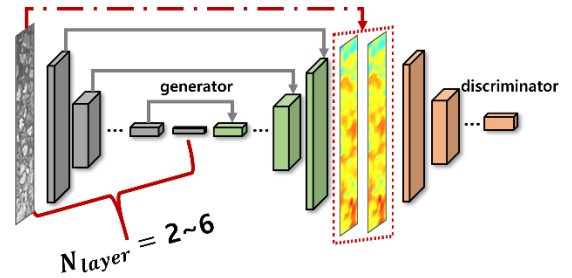


Fig. 1. Schematic representation of the ablation study on the generator structure of cGANs

The basis for the generator architecture is as follows:

Table II: Generator Architecture (encoder, decoder)

Layer	Input Channel	Output Channel	Kernel Size	Stride	Padding	Normalization	Dropout
1	3	64	(4,3)	(2,1)	(1,0)	False	-
2	64	128	(3,3)	(2,2)	(1,1)	True	-
3	128	256	(3,3)	(2,2)	(1,1)	True	-
4	256	256	(3,3)	(2,2)	(1,1)	True	0.5
5	256	256	(3,3)	(2,2)	(0,1)	True	0.5
6	256	256	(2,2)	(2,1)	(0,0)	True	0.5

The encoder and the decoder have the same structure to compress the input the latent variable and the expand it to generate the images, and the layers were chosen based on the depth, starting from layer (1,2), (1,2,3),

(1,2,3,4), (1,2,3,4,5) and (1,2,3,4,5,6), whose number ranges from 2 to 6, as in the Table II.

3. Results and discussion

3.1 Ablation of the neural network architecture

In each instance, modifications to the U-Net architecture impact the networks' spatial representations. Specifically, as the layered structure of the U-Net architecture, through skip connections, allows the model to retain spatial information, alterations in the layer count can affect its predictive capabilities. Fig. 2 illustrates the conversion of total reflection images into infrared images, highlighting the outcomes associated with varying numbers of layers.

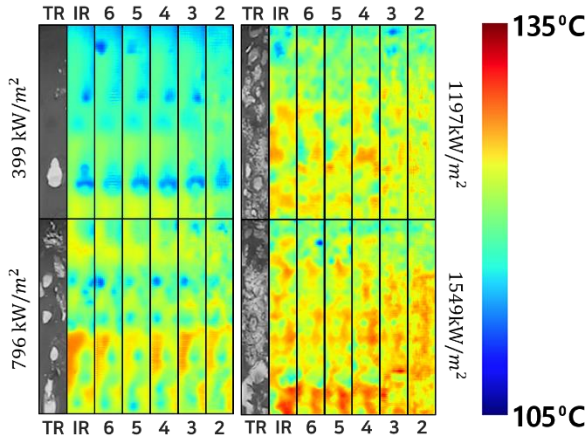


Fig. 2. Snapshots of the generated images at various heat fluxes and network depths

To quantify the model's accuracy, two image quality metrics were employed: Peak Signal-to-Noise Ratio (PSNR) and Structural Similarity Index Measure (SSIM). PSNR is defined as follows:

$$PSNR = 10 \log_{10} \left(\frac{MAX_I^2}{MSE} \right),$$

$$MSE = \frac{1}{MN} \sum_{i=0}^{M-1} \sum_{j=0}^{N-1} [I(i,j) - \hat{I}(i,j)]^2$$

Here, MAX_I represents the maximum pixel value of the image, and MSE denotes the mean square error between the original and reconstructed images, with M and N as the dimensions of the image.

SSIM assesses the combination of luminance, contrast, and structure and is defined as follows [8]:

$$SSIM(I, \hat{I}) = \frac{(2\mu_I\mu_{\hat{I}} + C_1)(2\sigma_{I\hat{I}} + C_2)}{(\mu_I^2 + \mu_{\hat{I}}^2 + C_1)(\sigma_I^2 + \sigma_{\hat{I}}^2 + C_2)}$$

Where μ_I and $\mu_{\hat{I}}$ are the means, σ_I^2 and $\sigma_{\hat{I}}^2$ are the variances of the original and reconstructed images,

respectively, and $\sigma_{I\hat{I}}$ is the covariance. Constants $C_1 = (k_1L)^2$, $k_1 = 0.01$, $k_2 = 0.03$, $L = 255$ are used. The image quality metrics of the test data are shown in Fig. 3.

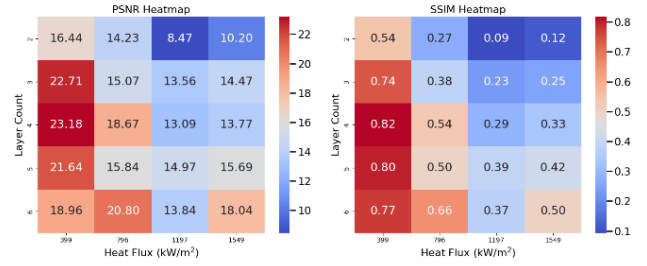


Fig. 3. Heatmap of the average image quality metrics of the test

The optimal complexity of neural networks is directly indicative of the data complexity, as additional layers cease to enhance performance once the optimum is reached. One of the primary reasons additional layers are not needed in a neural network is due to the risk of overfitting. The model learned the training data too well, capturing even noise or random fluctuations in the data instead of underlying distribution. This is effectively demonstrated in Fig. 3, where, at a low heat flux of 399 kW/m² and the flow boiling still in the single-bubble regime, as the system's complexity was significantly lower than at a higher heat flux of 1549 kW/m², which was more disordered and chaotic. Therefore, this lower complexity is directly reflected in the superior performance of the neural networks with a 4-layer structure at the lower heat flux, while the results of the 5-layer and 6-layer networks produced unnecessary artifacts of low-temperature area at the top of the image. Conversely, at 1549 kW/m², an increase in the number of layers directly benefited the neural networks' accuracy, highlighting the alignment between system complexity and network architecture.

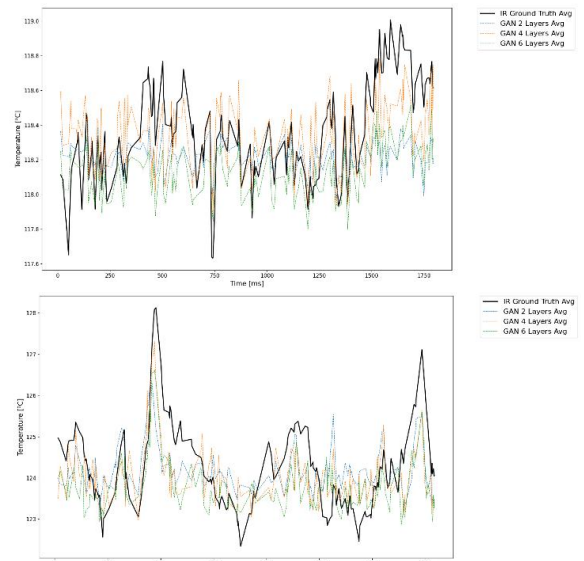


Fig. 4. Temperature evolution at $q = 399 \text{ kW/m}^2$ & 1549 kW/m^2

Fig. 4 displays the variations in average temperature over time for heat fluxes of 399 kW/m² and 1549 kW/m². At the lower heat flux, the mean squared error (MSE) of the average temperature was under 0.1°C, which is less than IR measurement uncertainty = 0.1°C. This suggests that the model can accurately predict average temperatures close to the actual values, indicating the neural network's ability to discern the temperature distribution patterns embedded within the total reflection images. Given the complexity of the problem, it is notable that the model provides a reasonable approximation of the temperature distribution.

4. Conclusions

This study introduced a new approach to understand the temperature field in flow boiling experiments using cGANs. This method simplifies the generation of temperature fields associated with infrared thermography by learning the temperature distribution tied to bubble dynamics, thereby accelerating the extraction of information from experimental data. Through an analysis of temperature field changes, the effectiveness of U-net-based generative models was evaluated, and the system's complexity was examined. Overall, the U-nets provided highly accurate average temperature estimates and reliable outcomes for local details. Future research might extend the application of this neural network model to unexplored areas, such as microchannels or non-penetrable surfaces.

5. Acknowledgement

This work was supported by Korea Hydro & Nuclear Power Co and Local Government (Pohang). (2024)

REFERENCES

1. Kim, S.H., et al., *Mechanism study of departure of nucleate boiling on forced convective channel flow boiling*. International Journal of Heat and Mass Transfer, 2018. **126**: p. 1049-1058.
2. Choi, M., et al., *Direct observation of rewetting failure mechanism at CHF under different subcooled flows*. International Journal of Heat and Mass Transfer, 2020. **163**: p. 120465.
3. Jeon, B.G., et al., *Observation of departure from nucleate boiling under flow using optical visualization and IR thermometry*. International Journal of Heat and Mass Transfer, 2022. **185**: p. 122417.
4. Krizhevsky, A., I. Sutskever, and G.E. Hinton, *Imagenet classification with deep convolutional neural networks*. Advances in neural information processing systems, 2012. **25**.
5. Goodfellow, I., et al., *Generative adversarial networks*. Communications of the ACM, 2020. **63**(11): p. 139-144.
6. Radford, A., L. Metz, and S. Chintala, *Unsupervised representation learning with deep convolutional generative adversarial networks*. arXiv preprint arXiv:1511.06434, 2015.
7. Isola, P., et al. *Image-to-image translation with conditional adversarial networks*. in *Proceedings of the IEEE conference on computer vision and pattern recognition*. 2017.
8. Wang, Z., et al., *Image quality assessment: from error visibility to structural similarity*. IEEE transactions on image processing, 2004. **13**(4): p. 600-612.